applied sciences

Article

Analysis of Cavity Corner Geometry Effect on Recirculation Zone Structure

Justas Šereika *, Paulius Vilkinis and Nerijus Pedišius

Laboratory of Heat-Equipment Research and Testing, Lithuanian Energy Institute, Breslaujos Str. 3, LT-44403 Kaunas, Lithuania; paulius.vilkinis@lei.lt (P.V.); nerijus.pedisius@lei.lt (N.P.)
* Correspondence: justas.sereika@lei.lt

Abstract: A numerical investigation of flow topology in open-type cavities with length-to-depth ratio L/h_1 = 4 was performed in the Reynolds number range of 10–1000. Cavities with differently rounded corners were chosen for simulation. Three-dimensional numerical simulations were performed to analyse flow topology in different planes. A series of experiments was performed to ensure the validity of numerical simulations. Both numerical simulations and physical experiments were conducted with water as the working fluid. Since the results agreed acceptably, further simulations were performed. The main goal of this study was to investigate and highlight the influence of rounded cavity corners on the topology and stability of flow. Analysis revealed that fully rounded upper cavity corners decrease pressure loss compared to other investigated cases; therefore, the velocity of the main flow is increased. Additionally, fully rounded upper corners form a notably smaller recirculation zone compared to other investigated cases. Flow stability analysis showed that fully rounded cavity bottom corners negatively impact flow stability by increasing the intensity of turbulence.

Keywords: CFD; cavity flow; flow topology; open-type cavity

Citation: Šereika, J.; Vilkinis, P.; Pedišius, N. Analysis of Cavity Corner Geometry Effect on Recirculation Zone Structure. *Appl. Sci.* **2022**, *12*, 6288. https://doi.org/10.3390/app12126288

Academic Editor: Francesca Scargiali

Received: 8 June 2022
Accepted: 17 June 2022
Published: 20 June 2022

1. Introduction

Research of fluid dynamics in channels with sudden expansion and contraction is common due to its simple geometry and complex physics, including widely known phenomena such as Taylor–Görtler vortices, corner and longitudinal vortices, the complex transition from laminar to turbulent flow, complex heat exchange processes, etc. Moreover, these phenomena have practical application, such as in aeronautics, automobile aerodynamics, and other industrial applications.

It is generally agreed to classify channels with sudden expansion and contraction into three types: open-type cavity ($L/h_1 < 10$), transitional-type cavity ($10 < L/h_1 < 13$) and closed-type cavity ($L/h_1 > 13$) [1]. Numerical and experimental investigations of fluid dynamics in open-type cavities are frequent in fluid dynamics research; therefore, many studies have been performed to deepen the fundamental knowledge of separated flow dynamics. Cheng and Hung [2] employed the lattice Boltzmann method to investigate vortex structure in a two-dimensional, lid-driven open-type cavity with a wide range of cavity length-to-depth ratios (L/h_1) and Reynolds numbers (Re). The study focused on vortex structure, revealing that when $L/h_1 \leq 1$, vortex structure is strongly dependent on Re. When Re $\leq$ 100, the cavity is filled with a large vortex alongside a pair of bottom corner vortices. As Re increases further, the sizes of the bottom vortices start to differ. However, when $L/h_1 < 1$, the number of vortices formed in the cavity increases with further L/h_1 decrease and Re increase. Another study of flow visualization in an open-type cavity was performed by Faure et al. [3]. The study was focused on flow visualization in the moderate Reynolds number range (1150–10,670) and varying cavity length-to-step-height ratio (L/h_1 = 0.5–2) of the shear-layer driven cavity. Analysis revealed that shear-layer secondary instabilities do not cause 3D developments, and that a secondary vortex in the upstream part of the cavity is linked to instability of the main vortex when $L/h_1 = 2$.

It is well known that studies of flow dynamics are inherent from heat transfer studies since heat exchange heavily relies on recirculation zone dynamics. Heat transfer has already been deeply analyzed in open-type cavities. Bilgen and Oztop [3] investigated heat transfer in flow driven by natural convection with ambient fluid in open-type, partially closed cavities with length-to-depth ratio $L/h_1 = 1$. The study showed that Nusselt number (Nu) depends on Rayleigh number (Ra), aspect ratio and aperture position. Additionally, the study showed that inclination angle had a nonlinear effect on heat transfer. A similar study was performed by Muftuoglu and Bilgen [4], where natural convection heat transfer in open-type cavities with a discrete heat source was investigated. The authors determined the optimal position of a discrete heater and its dependence on Ra. Further, the influence of geometrical parameter changes was determined on Ra and Nu by investigating various aspect ratios of the channel. It was shown that Ra is a decreasing function of the cavity aspect ratio, and that Nu is an increasing function of Ra. Prakash et al. [5] studied the effects of shape, wall temperature, cavity opening ratio and inclination on convective loss in open-type cavities. The study showed that the highest convective loss is observed in a hemispherical open-type cavity with opening ratios of 0.25 and 0.5. Additionally, the study showed that convective loss could be decreased by inclining the channel. The highest convective loss was observed at 0° inclination (horizontal channel) and the lowest at 90° (vertical channel). Laouira et al. [6] investigated mixed convection in a trapezoidal open-type cavity with a heat source of different lengths fixed to the bottom wall. The study showed that the highest Nu corresponded to the longest heat source, and that enhancement of heat transfer led to velocity distribution change in the cavity.

Since flow structure and topology in open-type cavities have already been thoroughly investigated, recent studies have focused on the impact of minor geometrical features on flow. Das and Cohen [4] numerically and experimentally investigated flow in an open-type cavity with $L/h_1 = 3.58$ to reduce pressure oscillations and noise by changing the rear face geometry of the cavity. Experiments were performed alongside two-dimensional numerical simulations with a Mach number of 0.9. The study revealed that softening of flow impact on the rear face leads to smaller pressure variations between the cavity's internal and external flow at the point of flow impact. A similar study was performed by Choi et al. [5] in a channel with an inclined backwards-facing step (BFS) whose inclination varied from 10° to 90°. Numerical study showed that the recirculation zone length remained constant in the turbulent flow regime at Re above 15,000 when the step angle was increased above 30°. Mushyam and Bergada [6] also studied laminar flow over an inclined step; numerical study showed that recirculation zone length strongly depends on Reynolds number. Yet no significant effect was noticed for step inclination at all angles. Decreased recirculation zone length was achieved by Bravo et al. [6] in a study where the distributions of mean flow and turbulence over a single rounded step were explored. Numerical investigation showed a shorter recirculation zone than for a channel with 90° BFS. Wu et al. [7] showed that the flow topology behind the BFS could also be impacted by increasing the roughness of the step's surface. A thorough experimental investigation was performed by Wu et al. to study the impact of realistic roughness topographies on turbulence, changing the surface of the step from a rough wall to a smooth wall. The study showed that step roughness influences recirculation zone length; secondary vortices were smaller when the surface of the step wall was rough. Measured shear stress suggested that turbulence can be weakened by increasing roughness.

A brief literature survey showed that studies of flow topology in open-type cavities are saturated. However, it was noticed that the impact of small geometry changes on flow structure and topology receives more interest nowadays. There are a decent number of studies on the influence of flow over differently shaped steps. Most are performed in channels with BFS or turbulent flow. To the authors' knowledge, there are no studies on flow topology in open-type cavities with rounded steps in laminar flow; therefore, this is a new fundamental interest and brings novelty to this research topic. The physical meaning of this study is to provide fundamental knowledge of the impact of geometry on recirculation zone dynamics, thus granting the necessary expertise for engineering solutions for various practical applications. The main goal of this study is to investigate the influence of rounded cavity corners on the topology and stability of laminar flow.

In this study, flow topology was numerically investigated by employing commercially available Ansys Fluent software. Results of numerical simulations were compared to experimental results to ensure the validity of simulations. Since the results agreed acceptably, further simulations were performed with four different geometries to determine the influence of rounded cavity corners on flow topology. For parametric analysis, pressure loss dependency on Re was obtained. Additionally, velocity profiles in x–y and x–z planes were obtained for all investigated channels. Finally, flow stability was investigated by analyzing Tu distribution in the cavities and C_f distribution on the bottom cavity wall.

2. Materials and Methods

2.1. Physical Model and Boundary Conditions

Four open-type cavities with differently rounded corners were chosen for numerical simulations (Figure 1). Ch1 is the classic case of an open-type cavity with two 90° steps. Ch2 and Ch4 have fully rounded and half-rounded bottom cavity corners, described as R = 0.3 mm and R = 0.15 mm, respectively. Conversely, only the top corners of cavity steps are fully rounded in Ch3, with R = 0.3 mm. Geometric dimensions given in Figure 1 (Ch1) apply to all investigated cavity cases. All investigated geometries were three-dimensional, with channel width b = 0.9 mm. Expansion and aspect ratios were fixed at ER = 2 and AR = 3, respectively.

Numerical simulations performed in this study involve water flow in the Re range of 10 < Re < 1000. The fluid is supposed to be incompressible with constant physical properties as follows: inlet temperature T = 288.16 K; dynamic viscosity $\mu = 1.003 \cdot 10^{-3}$ kg/m·s; density $\rho = 998.2$ kg/m^3.

The flow velocity profile is considered flat at the inlet; however, the inlet section is set to be 50 hydraulic diameters long before entering the cavity to ensure fully developed flow. A no-slip condition was assumed for the channel walls. Additionally, constant static pressure was set at the outlet boundary.

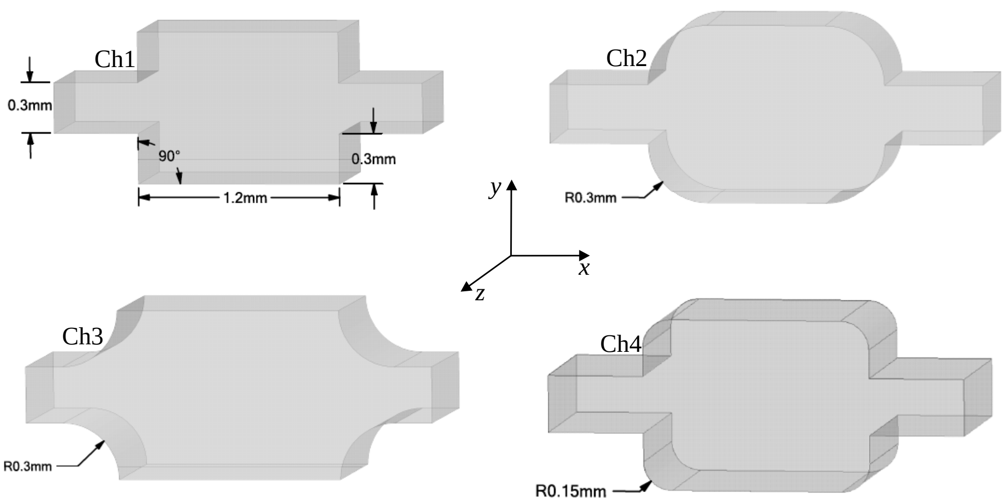

Figure 1. Investigated channels with given dimensions.

2.2. Computational Approach Using Ansys Fluent

Numerical simulations were performed using commercially available Ansys Fluent 2019 R2 (Ansys, Canonsburg, PA, USA) software with a 3D double-precision solver. The two-equation k–ε model was employed since it offers competitive efficiency and wide usage compared to other Reynolds-averaged Navier–Stokes (RANS) models [8]. Further, the standard wall function was used due to its significant reduction in computational expense. The pressure-based solver used the semi-implicit method for pressure-linked equations (SIMPLE) segregated algorithm, which applies corrections to the pressure field using the continuity equation. Additionally, a second-order upwind scheme was applied to discretize the momentum equation. The simulations were performed with a convergence criterion of 10^{-6} for continuity.

The standard k–ε turbulence model can be expressed as two equations as follows:

For turbulent kinetic energy k:

$$\frac{\partial(\rho k)}{\partial t}+\frac{\partial(\rho k u)}{\partial x}=\frac{\partial}{\partial x}\left[\left(\mu+\frac{\mu_t}{\sigma_k}\right)\frac{\partial k}{\partial x}\right]+G_k+G_b-\rho\varepsilon-Y_m+S_k; \tag{1}$$

For dissipation ε:

$$\frac{\partial(\rho\varepsilon)}{\partial t}+\frac{\partial(\rho\varepsilon u)}{\partial x}=\frac{\partial}{\partial x}\left[\left(\mu+\frac{\mu_t}{\sigma_\varepsilon}\right)\frac{\partial \varepsilon}{\partial x}\right]+C_{l\varepsilon}\frac{\varepsilon}{k}(G_k+C_{l\varepsilon}G_b)-C_{2\varepsilon}\rho\frac{\varepsilon^2}{k}+S_k; \tag{2}$$

where G_k and G_b—the generation of turbulence kinetic energy due to the mean velocity gradient and buoyancy, respectively; Y_m—contribution of the fluctuating dilatation in compressible turbulence to the overall dissipation rate; S_k and S_ε—user-defined source terms; σ_k and σ_ε—Prandtl numbers for k and ε, respectively; $C_{1\varepsilon}$, $C_{2\varepsilon}$ and $C_{3\varepsilon}$ are adjustable constants. Constant values of adjustable constants were used: $C_{1\varepsilon}$ = 1.44; $C_{2\varepsilon}$ = 1.92; $C_{3\varepsilon}$ = −0.33; σ_k = 1; σ_ε = 1.3.

Several grids of different cell densities were tested to ensure grid independence, with a step-height-to-cell-size ratio range of $7 < h_1/\Delta < 43$. A mesh independence test was performed at Re = 1000, and pressure difference was chosen as the reference parameter (Figure 2). As cell size decreased, the average relative change of pressure difference between inlet and outlet increased, becoming less dependent on cell size. Therefore, to perform computationally economic calculations, the grid was chosen at the point where average total pressure was no longer dependent on cell size. As a result, relative cell size was chosen $h_1/\Delta_c \approx 21.43$.

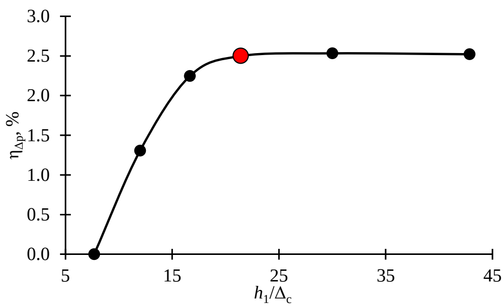

Figure 2. Mesh independence test.

2.3. Experimental Facility and Instrumentation

Velocity fields were experimentally measured using a micro-particle image velocimetry system (µPIV). The principal scheme of the µPIV system is given in Figure 3. During the experiments, laser illuminated fluorescent particles were captured by a CCD camera. The results were obtained as flow velocity vector fields calculated from changes in particle location over a specified time interval. As shown in Figure 3., laser beam was directed toward the microscope, where it was reflected by 90° due to the dichroic mirror installed inside the microscope. The laser beam was then directed through the microscope lens, which directly concentrated the light to the experimental section. A dichroic mirror also ensured the specific wavelength required to excite fluorescent particles and filter light travelling towards the CCD camera.

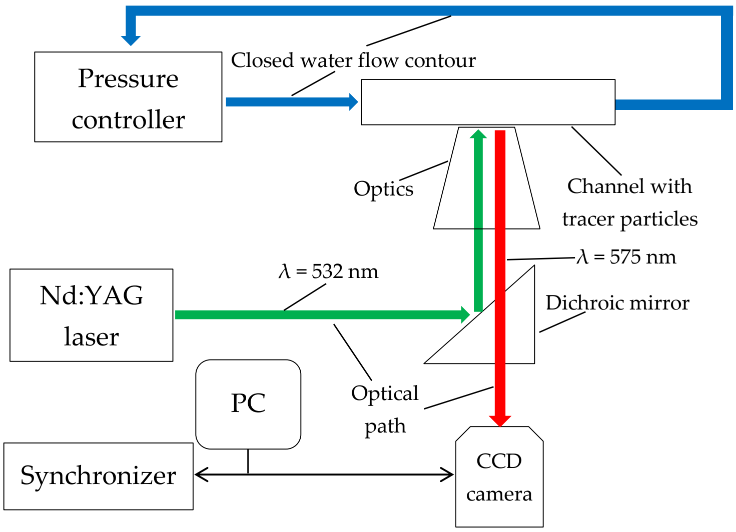

Figure 3. Principal scheme of µPIV system.

The µPIV facility consisted of an Elveflow OB1 MK3 (Elveflow, Paris, France) pressure controller, a Nd:YAG type dual-cavity laser and a 2048 × 2048 pixel FlowSense EO CCD camera (Dantec Dynamics, Skovlunde, Denmark) coupled with an inverted Leica DM ILM microscope (Leica Microsystems, Wetzlar, Germany). The FlowSense EO CCD camera has a pixel size of 7.4 µm and provides a field of view of approximately 1.5 × 0.6 mm at 10× image magnification. For device control and image analysis, DynamicStudio v6.11 (Dantec Dynamics, Skovlunde, Denmark) software was employed. The image pairs of fluid flow with tracer particles were captured at 15 Hz frequency with the time interval between consecutive images ranging from 1 µs to 500 µs depending on Re. Time-averaged results were obtained by averaging no less than 200 images.

Water was chosen as the working fluid, with 1 µm diameter fluorescent particles (Invitrogen, Waltham, MA, USA). Flow was created using a programmable pressure controller, ensuring steady channel inlet pressure. The specific gravity of fluorescent particles was 1.05; therefore, flow was considered single-phased, and Brownian motion was avoided. Laser excitation and emission wavelengths were 535 nm and 575 nm, respectively. Additionally, water temperature was ensured to be 21 ± 1 °C during experiments. Experimental channels were manufactured in polycarbonate, with the preferred channel geometry engraved into them. Cavity geometry Ch4 (Figure 1) was chosen as an experimental object. Before entering the cavity, flow was ensured to be fully developed by making the inlet length 50 hydraulic diameters long.

The uncertainty of velocity measurements was determined by assessing the contribution of expanded uncertainty of pressure-control-unit generated flow, channel cross-section dimensions, the uncertainty in the correlation calculation due to its dependence on the selected time-period between image pairs and the uncertainty of velocity measurement repeatability. Analysis revealed that the expanded uncertainty of velocity measurement by µPIV did not exceed 7%.

2.4. Numerical and Experimental Result Comparison

Numerically and experimentally obtained flow distribution results in Ch4 are compared in Figures 4 and 5. The results show acceptable agreement. However, it should be noted that as Re increased and the flow started to enter transitional flow, flow instabilities increased; therefore, the ability to numerically predict separated flows weakens due to underestimated turbulent kinetic energy generated by flow separation [9–13]. This phenomenon is also observed in the numerical simulations, where for Re = 1000, CFD predicted higher reverse flow velocities (Figure 5).

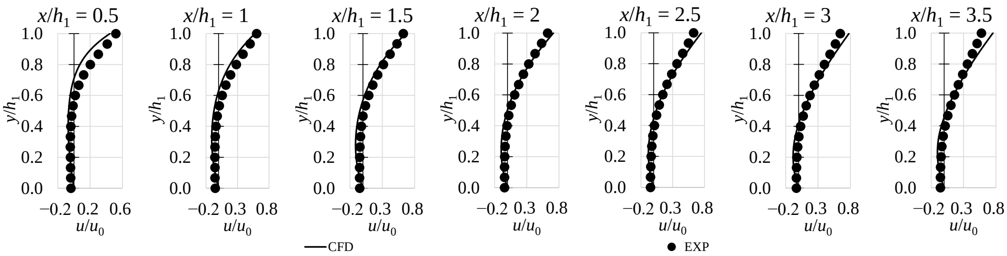

Figure 4. Numerically and experimentally obtained velocity u profiles at Re = 100.

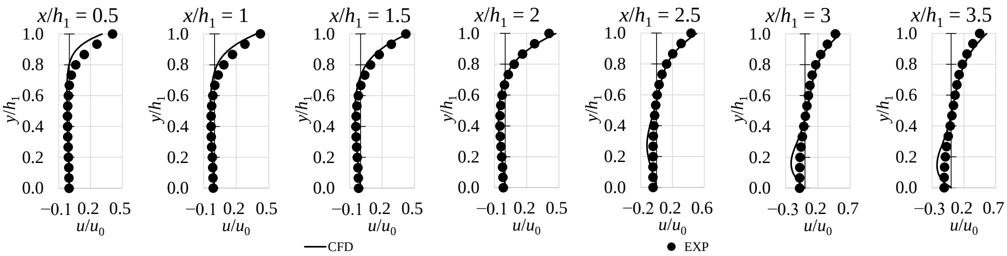

Figure 5. Numerically and experimentally obtained velocity u profiles at Re = 1000.

3. Results and Discussion

3.1. Investigation of Flow Topology in the x–y Plane

Flow topology in the x–y plane is represented as static pressure contours with flow velocity streamlines in Figure 6. Formation and dynamics of the recirculation zone depend on cavity geometry and Re.

In general, recirculation zone length increases as Re increases. Depending on cavity geometry, the recirculation zone at Re = 10 exists in all cases except Ch3. The recirculation zone is the longest in Ch1, decreases in Ch4 and Ch2, and is absent in Ch3. Rounding of cavity bottom corners causes a lower pressure gradient; therefore, a weaker recirculation zone forms compared to the sudden cross-section changes in Ch1. In Ch3, due to rounded upper cavity corners and smooth transition from the channel to the cavity, streamlines follow cavity geometry smoothly and enter the cavity without separation.

As Re increases (Re = 100), the recirculation zone becomes of comparable size and shape. Due to an increase of the main flow velocity, more kinetic energy is transferred to the recirculation zone, forcing it to grow. Yet in Ch3, the recirculation zone is still weakest. The pressure gradient is sufficient for the shear layer to separate; however, it is not sufficient for the recirculation zone to fill the entire cavity, thus reattachment is observed near the trailing wall. Because of the smaller recirculation zone, the main flow impingement occurs lower on the trailing wall compared to other cases. The impingement location matches the location of maximum pressure on the trailing cavity wall. Due to a shorter recirculation zone, maximum pressure values are distributed over a larger area on the trailing wall compared to other cases. As the cavity is filled with the recirculation zone, the separated shear layer bridges the cavity, and impingement occurs on the trailing wall edge.

Additionally, flow topology changes are observed at Re = 1000. In this case, recirculation zones have reached their final shape and no longer depend on Re. The main difference from Re = 100 cases is the shift of vortex centre position to the vicinity of the trailing wall. In such flow, force is balanced between the main flow in the channel and the recirculation flow in the cavity. Concerning heat transfer enhancement in investigated geometries, Ch3 seems to be most promising due to the longest-lasting shear layer reattachment and the most unstable recirculation zone, especially at higher Re.

Additionally, corner eddies (known as Moffat eddies) located between the leading cavity wall and the recirculation zone are formed in Ch1. The length of corner eddies is measured by the wall shear stress on the cavity bottom. The presence of corner eddies is due to an adverse pressure gradient behind the leading wall [14]. The minimum wall shear stress values are associated with the beginning and the end of the eddy. The distribution of wall shear on the

Ch1 bottom is given in Figure 7a. Note that the lengths of corner eddies in all investigated Re cases are tiny; therefore, they are not visible in Figure 6. In Ch1, the size of the corner eddy increases with increasing Re in similar manner to the main recirculation zone (Figure 7b). It is well known that fluid flow through a corner that is greater than 73.5° creates Moffat eddies [15]; therefore, corner eddies do not form for the rounded cavity corners (Ch2 and Ch4) (Figure 6). Additionally, corner eddies in Ch3 are absent due to gradually rounded corners—the adverse pressure gradient is insufficient for flow separation, and streamlines follow the corner geometry without forming recirculation zones.

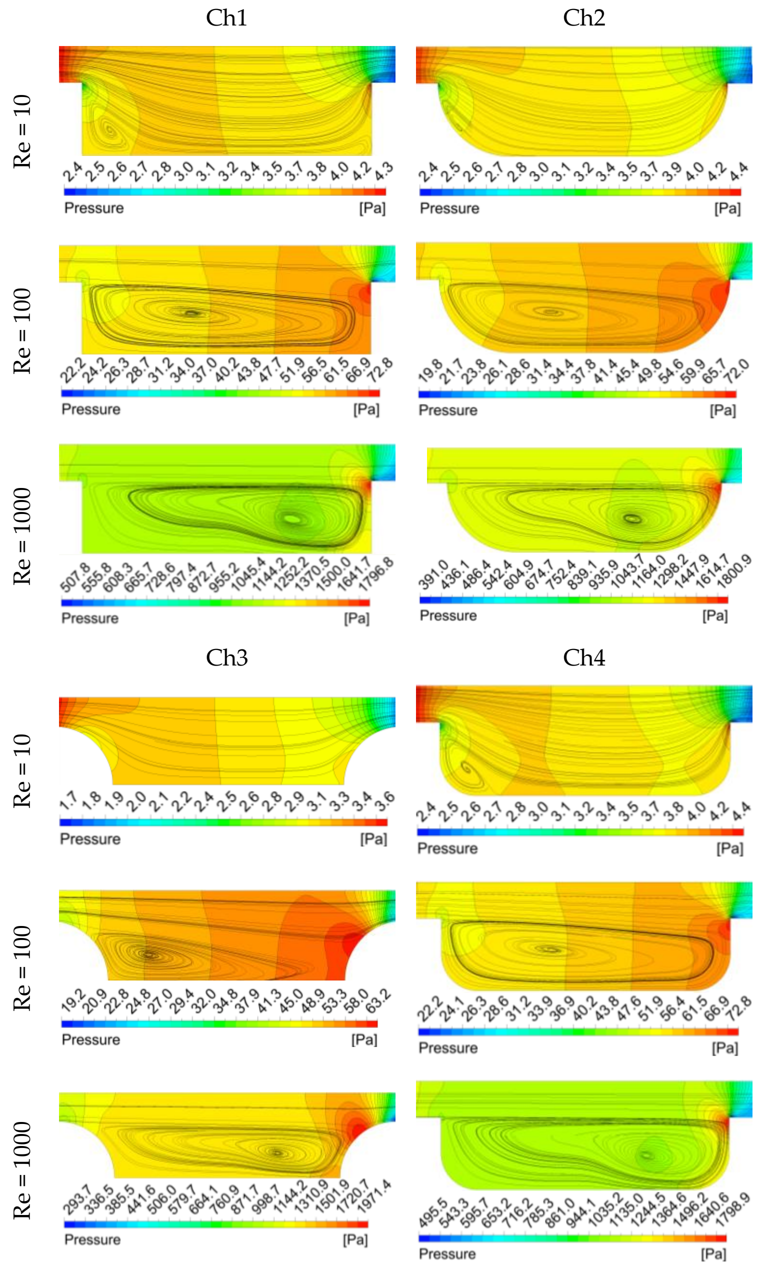

Figure 6. Static pressure contours and velocity streamlines in Ch1, Ch2 and Ch3 at Re = 10, 100 and 1000.

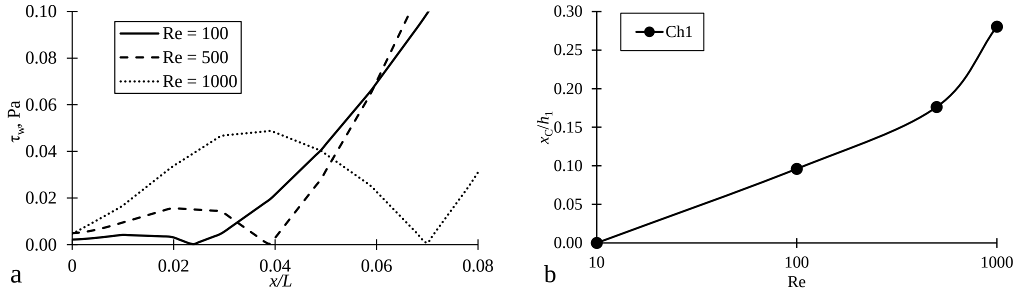

Figure 7. Wall shear distribution on the bottom of Ch1 (**a**) and x_C dependency on Re (**b**).

Flow velocity u profiles in Ch1, Ch2 and Ch3 are given in Figures 8 and 9. The profiles are measured along the cavity in the middle plane at equal distances of $0.5h_1$. The velocity profiles of Ch4 are not presented since they are identical to Ch1. As can be seen, velocity profiles in Ch1 and Ch2 coincide in most cases. Slight differences are observed only at the beginning of the cavity and near the trailing wall due to different corner rounding radii. In Ch2 at Re = 100 (Figure 8), the recirculation zone is affected by a gradually decreasing channel cross-section. Therefore, the interaction between the main flow and recirculation zone is strengthened, causing a stronger recirculation zone at $0.3 < y/h_1 < 0.75$. Higher u velocities along the cavity in Ch3 at Re = 100 are determined by a shorter and weaker recirculation zone. As Re increases, velocity profiles coincide well because flow structure in the cavity is stable and small changes in cavity geometry have a diminishing influence on flow structure.

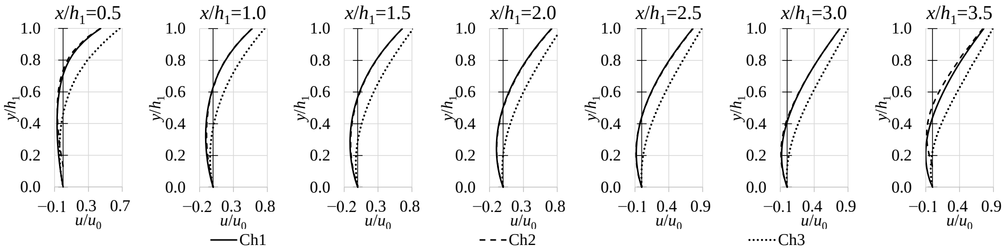

Figure 8. Velocity u profiles in Ch1, Ch2 and Ch3 at Re = 100.

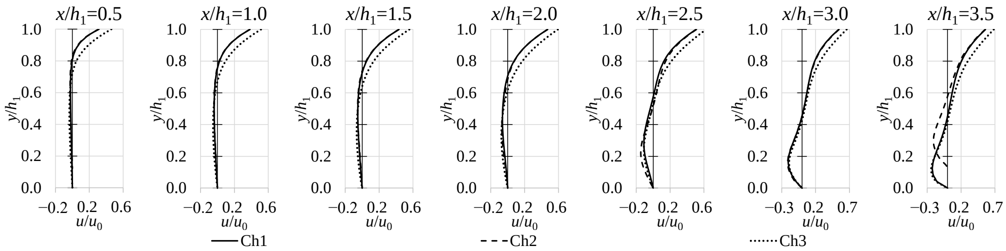

Figure 9. Velocity u profiles in Ch1, Ch2 and Ch3 at Re = 1000.

The most significant geometry impact is observed in Ch3 at Re = 100, where the recirculation zone is weaker and a thinner reverse flow layer is observed compared to other cases. The highest velocity values are observed when Re $\geq$ 100 due to the lowest pressure losses. Figure 10 gives pressure loss dependency on Re. Pressure loss is calculated as the difference between inlet and outlet pressure. As can be seen, pressure losses in all cases are similar at low Re. As Re increases, pressure losses remain similar in Ch1 and Ch2; however, decreased pressure losses are observed in Ch3, as could have been foreseen from the velocity fields and profiles presented above. The reduction of pressure losses due to cavity corner rounding could serve as a roadmap in designing specific applications.

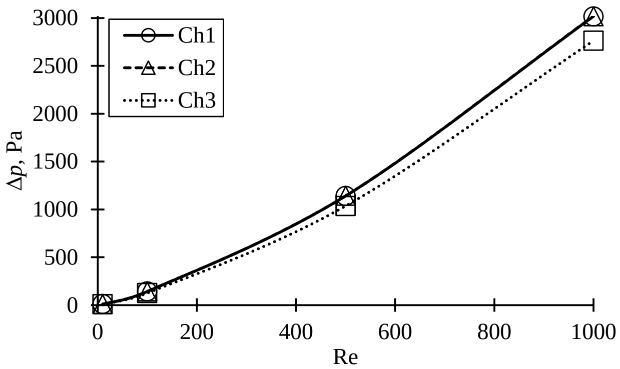

Figure 10. Pressure drop in Ch1, Ch2 and Ch3.

3.2. Investigation of Flow Topology in the x–z Plane

Flow streamlines and velocity u profiles measured in the x–y plane are given at $y/h_1 = 0.5$ (in Figures 11 and 12). At Re = 100, lateral vortices are observed in all investigated cases. Note that longitudinal dimensions differ in every investigated channel due to geometry limitations. For example, the growth of lateral vortices in Ch3 is determined by increased velocity in the centre of the channel; therefore, more kinetic energy is transferred to lateral vortices, thus increasing their size. Further, since the recirculation zone in Ch3 is smaller than in other cases, the difference in reverse flow distribution between Ch3 and Ch1/Ch2 is evident, as can be observed from the x–z plane velocity u profiles (Figure 12). In Ch3, the separated shear layer reattaches to the cavity bottom (Figure 6), and the recirculation zone is smaller than in other cases. Therefore, the effective flow cross-section increases in the cavity. Due to more space for flow development above the recirculation zone, the velocity at $y/h_1 = 0.5$ is more than three times greater than in other cases at the middle part of the cavity.

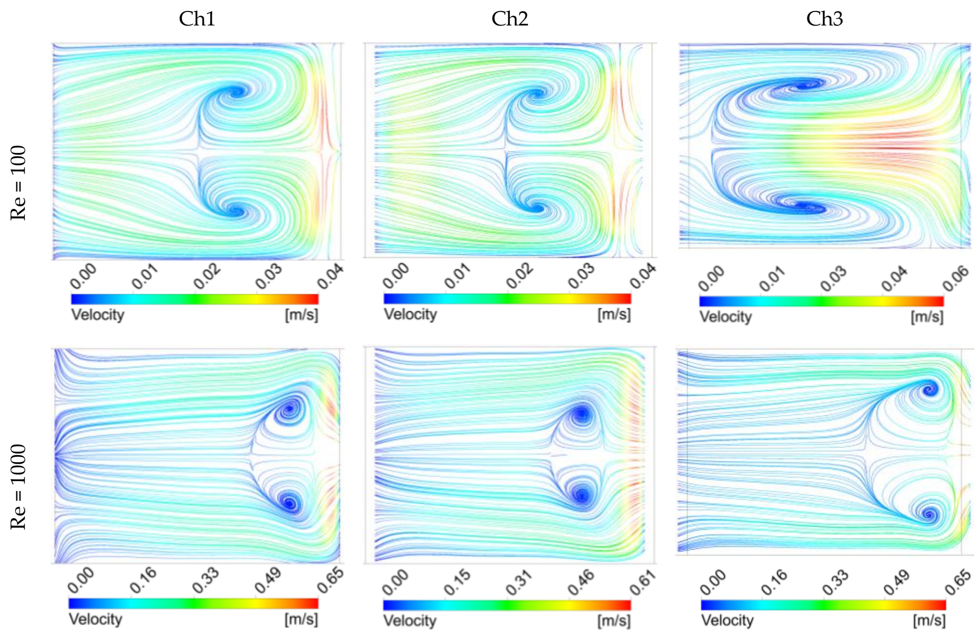

Figure 11. Velocity contours in the x–z axis.

When the flow approaches the trailing wall, the velocity differences between the investigated channels become lesser, yet are still notable. However, as the Re increases to Re = 1000, the impact of geometry on flow topology becomes less significant because recirculation zones become of comparable size. The lateral vortices formed near the leading wall are displaced towards sidewalls in Ch3 compared to Ch1/Ch2 because the trailing cavity wall is being bent inside the cavity, and from the resulting space restrictions the vortex centre is stretched across the cavity. A lesser effect is observed in Ch1. The opposite is observed in Ch2, where lateral vortices are close to each other and in the vicinity of the cavity mid-plane when the trailing wall is bent outside, and the vortex core is less restricted.

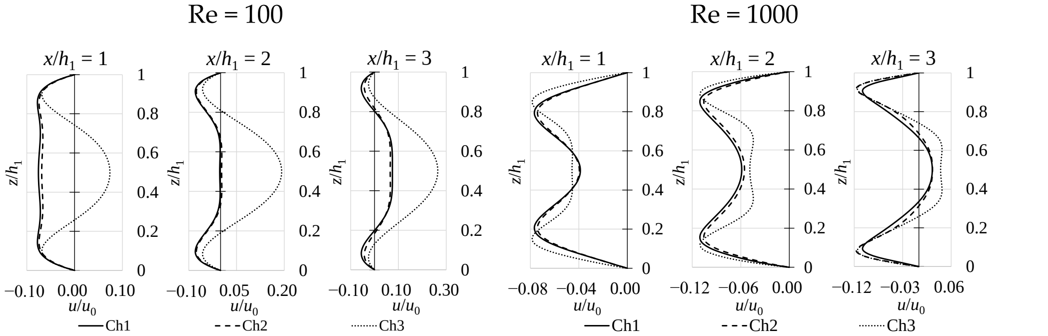

Figure 12. Velocity u profiles at the x–z plane height of y/h_1 = 0.5.

Turbulence intensity profiles at Re = 1000 are given in Figure 13. Re = 1000 is presented due to the flow structure being considered fully developed in the cavity. It is known that increased *Tu* values may cause flow instabilities and the presence of secondary flows [16]; therefore, the distribution of *Tu* is investigated to analyse flow stability.

Out of all investigated channels, the highest increase of *Tu* is observed in Ch2. This implies that the fully curved cavity bottom corners cause the flow to become less stable, i.e., the flow tends to fluctuate. Gradually decreasing the cross-section (near FFS) strengthens interactions between the recirculation zone centre and the main flow. Thus, flow perturbations near the recirculation zone centre occur; therefore, peak *Tu* is observed at x/h_1 = 3.5. This applies to Re = 500 and Re = 1000; therefore, its magnitude does not depend on Re. Additionally, increased *Tu* implies that the flow becomes less two-dimensional [17]. Conversely, the opposite situation is seen in Ch3, where *Tu* decreases in the recirculation zone, implying that the recirculation zone is more stable.

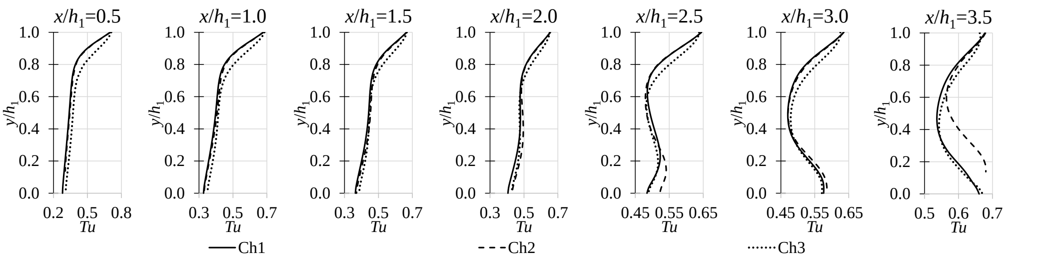

Figure 13. Turbulence intensity profiles along the cavity at Re = 1000.

3.3. Investigation of Flow Parameters Corresponding to Flow Stability

Skin friction coefficient C_f distribution on the cavity bottom wall is given in Figure 14. Increased C_f is associated with increased static pressure along the cavity. The minimum C_f is observed behind the leading cavity wall, where small secondary vortices or smooth streamlines are present depending on corner geometry. C_f abruptly increases with the beginning of the recirculation zone and reaches a plateau in Ch1 and Ch2 in the middle of the cavity at the recirculation zone centre. The Ch3 recirculation zone is not fully formed; therefore, Cf values are lower, and a plateau is not observed as the recirculation zone size decreases along the cavity, contrary to Ch1 and Ch2. A slight decrease in *Cf* is observed at *x/L* ~0.7 in Ch1 and Ch2 as the recirculation zone weakens along the cavity. In Ch3, *Cf* reduction is more pronounced due to shear layer reattachment to the cavity bottom. As the trailing wall of the cavity approaches, the favourable pressure gradient rapidly increases, leading to increased C_f. In Ch1 and Ch2, C_f distribution along the cavity is similar because of analogous recirculation zone dynamics. However, in Ch3, the adverse pressure gradient is lower at the inlet of the cavity; therefore, a weaker recirculation zone is formed, leading to lower flow resistance.

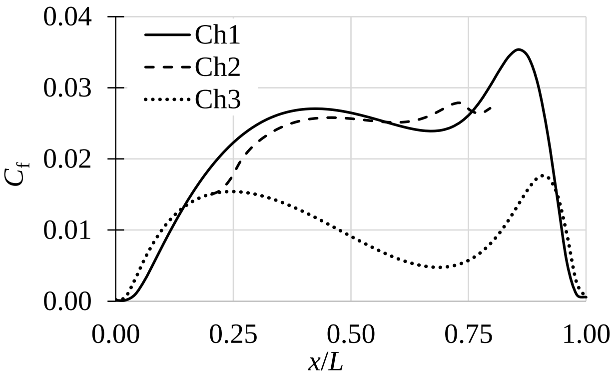

Figure 14. Skin friction coefficient at Re = 100.

4. Conclusions

In this study, dynamics of laminar flow in open-type cavities with differently rounded corner geometries were numerically investigated.

Investigation of recirculation zone structure based on cavity corner shape showed that corner geometry determines the size and number of vortices in the cavity. The strongest recirculation zone is formed in the right-angled cavity (Ch1), and vortex size decreases in half-rounded (Ch4) and fully rounded (Ch2) bottom corners and rounded upper (Ch3) corners due to a reduced adverse pressure gradient behind the leading cavity wall. Rounded corner type and radius also affect the location and size of the transverse vortex centre with respect to the side and trailing walls of the cavity.

Parametric analysis revealed that pressure losses are notably lower with rounded upper cavity corners (Ch3) due to reduced recirculation zone size and an increased effective flow cross-section. Flow stability analysis showed that fully rounded cavity corners (Ch2) negatively impact flow stability by increasing *Tu* near the trailing cavity wall. The gradually decreasing channel cross-section near the trailing wall strengthens the interactions between the recirculation zone and the main flow, causing flow perturbations to appear.

Broader analysis of flow structure on flow regime and investigation of heat transfer processes dependent on small changes to cavity geometry will be presented and discussed in forthcoming papers.

Author Contributions: J.Š.: Conceptualization, Validation, Investigation, Formal analysis and Writing. P.V.: Conceptualization, Investigation, Supervision and Writing. N.P.: Conceptualization, Resources and Project administration. All authors have read and agreed to the published version of the manuscript.

Funding: This research received no external funding.

Conflicts of Interest: The authors declare no conflict of interest.

Nomenclature

L	[m]	Cavity length;	Tu	[-]	Turbulence intensity, $Tu = \frac{\sqrt{u'^2}}{u_0}$
b	[m]	Cavity width;	u'	[m/s]	Longitudinal velocity fluctuation, $u' = \sqrt{\frac{1}{3}\left(u'^2 + v'^2 + w'^2\right)}$;
h_1	[m]	Step height;	Δ_c	[m]	Cell size;
h	[m]	Channel inlet/outlet height;	D_h	[m]	Hydraulic diameter, $D_h = \frac{2hb}{(h+b)}$;
H	[m]	Height of the channel in the cavity cross-section, $H = (h + h_1)$;	ER	[-]	Expansion ratio, $ER = \frac{H}{h_1}$;

u	[m/s]	x-axis velocity;	u_0	[m/s]	Inlet x-axis velocity;
v	[m/s]	y-axis velocity;	AR	[-]	Aspect ratio, $\mathrm{AR} = \left(\frac{b}{h}\right)$;
w	[m/s]	z-axis velocity	Re	[-]	Reynolds number, $\mathrm{Re} = \frac{u \times D_h}{\nu}$;
τ_w	[Pa]	Skin shear stress on a surface;	ν	[m^2/s]	Kinematic viscosity;
V	[m/s]	Velocity, $V = \sqrt{u^2 + v^2 + w^2}$;	C_f	[-]	Skin friction coefficient, $C_f = \frac{\tau_w}{\frac{1}{2}\rho v^2}$;

References

1. Tracy, M.B.; Plentovich, E.B. *Cavity Unsteady-Pressure Measurements at Subsonic and Transonic Speeds*; NASA, Langley Research Center: Hampton, VA, USA, 1997; Volume 3669.
2. Cheng, M.; Hung, K.C. Vortex Structure of Steady Flow in a Rectangular Cavity. *Comput. Fluids* **2006**, *35*, 1046–1062. [CrossRef]
3. Faure, T.M.; Adrianos, P.; Lusseyran, F.; Pastur, L. Visualizations of the Flow inside an Open Cavity at Medium Range Reynolds Numbers. *Exp. Fluids* **2007**, *42*, 169–184. [CrossRef]
4. Das, S.; Cohen, J. Effect of Rear Face Geometry on the Open Cavity Oscillatory Flow at M = 0.9. In Proceedings of the 8th AIAA Flow Control Conference, Washington, DC, USA, 13–17 June 2016; pp. 1–12. [CrossRef]
5. Choi, H.H.; Nguyen, V.T.; Nguyen, J. Numerical Investigation of Backward Facing Step Flow over Various Step Angles. *Procedia Eng.* **2016**, *154*, 420–425. [CrossRef]
6. Bravo, H.R.; Zheng, Y.H. Turbulent Flow over Step with Rounded Edges: Experimental and Numerical Study. *J. Hydraul. Eng.* **2000**, *126*, 82–85. [CrossRef]
7. Wu, Y.; Ren, H.; Tang, H. Turbulent Flow over a Rough Backward-Facing Step. *Int. J. Heat Fluid Flow* **2013**, *44*, 155–169. [CrossRef]
8. Shaheed, R.; Mohammadian, A.; Kheirkhah Gildeh, H. A Comparison of Standard k–ε and Realizable k–ε Turbulence Models in Curved and Confluent Channels. *Environ. Fluid Mech.* **2019**, *19*, 543–568. [CrossRef]
9. Dol, S.S. Particle Image Velocimetry Investigation of Steady Flow over a Backwardfacing Step. *EPJ Web Conf.* **2016**, *114*, 02018. [CrossRef]
10. Tihon, J.; Pěnkavová, V.; Havlica, J.; Šimčík, M. The Transitional Backward-Facing Step Flow in a Water Channel with Variable Expansion Geometry. *Exp. Therm. Fluid Sci.* **2012**, *40*, 112–125. [CrossRef]
11. Armaly, B.F.; Durst, F.; Pereira, J.C.F.; Schönung, B. Experimental and Theoretical Investigation of Backward-Facing Step Flow. *J. Fluid Mech.* **1983**, *127*, 473. [CrossRef]
12. Biswas, G.; Breuer, M.; Durst, F. Backward-Facing Step Flows for Various Expansion Ratios at Low and Moderate Reynolds Numbers. *J. Fluids Eng. Trans. ASME* **2004**, *126*, 362–374. [CrossRef]
13. Mohammad, A.; Hossain, M.; Taibur Rahman, S.R. Numerical Investigation of Fluid Flow through A 2D Backward Facing Step Channel. *Int. J. Eng. Res. Technol.* **2013**, *2*, 3700–3708.
14. Shen, F.; Xue, S.; Xu, M.; Pang, Y.; Liu, Z.M. Experimental Study of Single-Particle Trapping Mechanisms into Microcavities Using Microfluidics. *Phys. Fluids* **2019**, *31*, 042002. [CrossRef]
15. Moffatt, H.K.; Mak, V. Corner Singularities in Three-Dimensional Stokes Flow. In *IUTAM Symposium on Non-Linear Singularities in Deformation and Flow*; Springer: Dordrecht, The Netherlands, 1999; pp. 21–26; ISBN 9789401147361.
16. Ghorbanian, K.; Soltani, M.R.; Manshadi, M.D. Experimental Investigation on Turbulence Intensity Reduction in Subsonic Wind Tunnels. *Aerosp. Sci. Technol.* **2011**, *15*, 137–147. [CrossRef]
17. Isomoto, K.; Honami, S. The Effect of Inlet Turbulence Intensity on the Reattachment Process over a Backward-Facing Step. *J. Fluids Eng. Trans. ASME* **1989**, *111*, 87–92. [CrossRef]